



ORIGINAL RESEARCH ARTICLE

# Influence of High-Temperature Annealing on Microstructure and Properties of Welded Joints Using Narrow Gap Laser Welding of TC4 Titanium with Welding Wire

Mingqiu Wang, Pengbo Wu, Kai Xu, Ruisheng Huang, Xingxing Wang, Naiwen Fang, Laibo Sun, Jian Qin, Yiming Ma, and Jinhua Su

Submitted: 3 March 2023 / Revised: 11 June 2023 / Accepted: 4 August 2023

To solve the technical problems of poor strength–plasticity–toughness matching of titanium alloy welded joints, the optimized multi-stranded wires are used as the filler metal for narrow gap laser welding of TC4 titanium, and the welded joints obtained using high-temperature annealing were heat-treated at 850 °C holding 2 h. The macrostructure, microstructure and texture of both welded joints were compared by employing an optical microscope, scanning electron microscope and transmission electron microscope, and the tensile and impact properties were also evaluated. The results show that after heat treatment of the welded zone acicular  $\alpha'$  martensite decomposition into lamellar  $\alpha$ -phase +  $\beta$ -phase, the welded joint microhardness distribution tends to be smooth, the average tensile strength of the welded joints is 902 MPa, elongation is 14.5%, about 4.1% lower than the as-welded of the welded joints tensile strength, but elongation increased 3.5%, and room-temperature impact energy is 18.5 J, increased by about 54% than the as-welded impact energy, achieving a reasonable match of strength–plasticity–toughness of titanium alloy welded joints.

**Keywords** high-temperature annealing, laser filler wire welding, microstructure and properties, titanium alloy

## 1. Introduction

Titanium and titanium alloys are widely used in aerospace and aeronautics, marine engineering, and military applications due to their advantages in low density, superior strength-to-weight ratio, and excellent corrosion resistance properties (Ref 1-3). TC4 titanium alloy is an  $\alpha + \beta$  duplex-phase alloy, containing 6% of  $\alpha$ -phase stable element Al and 4% of  $\beta$ -phase stable element V, which have underpinned its excellent overall performance in ductility, toughness, and high-temperature resistance. Therefore, it is widely applied in key component manufacturing, such as structural parts of hulls, pressure-

resistant shells of deep submersibles, and engine compartments of aviation equipment (Ref 4-6).

However, titanium alloys are highly active and susceptible to oxidation during the welding process and thus prone to the formation of gas-rich layers, making welding a more difficult job (Ref 7-8). Traditional fusion welding of titanium alloys tends to cause problems like holes (Ref 9), cracks (Ref 10), distortions (Ref 11-12), and poor ductility (Ref 13) due to elongated high-temperature residence time for their high melting point, low thermal conductivity, and high thermal expansion coefficient, while narrow gap laser wire welding of titanium alloys could save us from all those troubles. This welding procedure requires low heat input, presents narrow heat-affected zone, and is highly efficient. It allows the addition of beneficial elements through filler wires, which also compensate for the loss of burned alloys. It is more adaptable to welding grooves with different forms and sizes and could effectively control welding stress and strain in the joints while ensuring its microstructure and properties (Ref 14-18). With its broad application prospects in joining titanium alloys with large thicknesses and complex structures, narrow gap laser wire welding technology will become one of the most advanced technologies in terms of the engineering applications of titanium alloys (Ref 19-20).

One problem when narrow gap laser welding with thick-wall titanium alloy wire feed is that welded joints' plasticity and impact toughness are hard to control (Ref 21-23). Since the  $\alpha$  phase, due to a large temperature gradient, shear transforms to acicular  $\alpha'$  martensite rather than diffusing fully and growing in the  $\beta$ -phase during the cooling process of the welded, post-weld heat treatment is an effective way to solve this problem and get high-quality welding joints. By controlling the temperature below the transition temperature of the  $\beta$ -phase to allow the full diffusion and decomposition of  $\alpha'$  martensite, the plasticity and toughness of welded joints can be fully guaranteed (Ref 24-26).

**Mingqiu Wang**, Shanghai Zhongxun Technology Co., Ltd., Shanghai 201200, China; **Pengbo Wu, Kai Xu, Ruisheng Huang, Naiwen Fang, Laibo Sun, Yiming Ma**, and **Jinhua Su**, Harbin Welding Institute Limited Company, Harbin 150028, China; **Xingxing Wang**, Henan International Joint Laboratory of High-Efficiency Special Green Welding, North China University of Water Resources and Electric Power, Zhengzhou 450045, China; and **Jian Qin**, Zhengzhou Research Institute of Mechanical Engineering Limited Company, Zhengzhou 450001, China. Contact e-mails: Shirley.wang@shzhongxun.com, wpbwelding@163.com, xkwelding@163.com, huangrs9@163.com, wangxingxing@ncwu.edu.cn, naiwen20@163.com, slb1984@126.com, qinjianzhu@163.com, myiming246@sina.com, and 13836130125@163.com.

Related studies have indicated that setting the annealing temperature between 600 and 850 °C would effectively promote the  $\alpha'$  martensite to diffuse and decompose, thus improving the plastic toughness (Ref 27). Another study showed that  $\alpha'$  martensite decomposition was easily observed when heat treatment was performed under 750-900 °C, which helped to improve the plastic toughness (Ref 28).

Using 1 × 3 twisted wire as filler metal and a defects-suppressing welding procedure, laser welding with wire feed of TC4 titanium alloy plate was performed in this paper. Our research team designed and developed the welding wire and the welding procedure. In order to optimize the strength–plasticity–toughness of the welded joints, a high-temperature annealing heat treatment at 850 °C/2 h was performed, and systematic analysis was followed up on the microstructure and properties of the joints as-welded and after heat treatment, respectively. This research could provide technical support for future laser welding applications with wire feed of titanium alloys.

## 2. Experimental Procedures

TC4 titanium alloy sheets with a thickness of 20 mm were used in this study. The chemical composition (in mass fraction) of TC4 titanium alloy was 6.25% Al, 4.10% V, 0.15% Fe, 0.028% C, and balance Ti, respectively. TC4 multi-stranded wire with 1 × 3 structure and 1.6 mm diameter was selected as

filler metal whose chemical composition (in mass fraction) was 6.20% Al, 3.92% V, 0.20% Fe, 0.028% C, and balance Ti, respectively. The plate to be welded was processed into a Y-groove before welding, with a groove blunt edge 2 mm, a groove root gap 3.2 mm, and a single-sided groove angle 1.5 °. The test plate to be welded was fabricated into a Y-shape groove, with a root face 2 mm, a root opening 3.2 mm, and a bevel angle 1.5 °. The butt joints of sheets were joined by circular oscillation narrow gap laser welding with wire feed, in which oscillating frequency and width were set at 100 Hz and 2 mm, respectively. Laser power, welding speed, welding wire feeding rate, and defocusing distance were 4000 W, 0.42 m/min, 3.5 m/min, and + 20 mm, respectively. The narrow gap laser welding was carried out with equipment, including FLW D50W scanning laser torch, Kuka robot, Fronius KD 1500 D-II wire feeder, and YLS-30000-S4 fiber laser. Argon was applied as shielding gas at a rate of 30 L/min. A schematic representation of the welding process is shown in Fig. 1.

To optimize the microstructures and mechanical properties of the TC4 titanium alloy welded joint, a high-temperature annealing (850 °C/2 h, furnace cooling) treatment was performed, followed by microstructure analysis and mechanical properties test. The metallographic sample of the welded joint was cut off perpendicularly to the weld, and a cross section was prepared for metallographic analysis by grinding, polishing, and corrosion resistance tests. The microstructure of the welded joint was examined via optical microscopy (OM, model: Olympus Cky53), scanning electron microscopy (SEM, model:

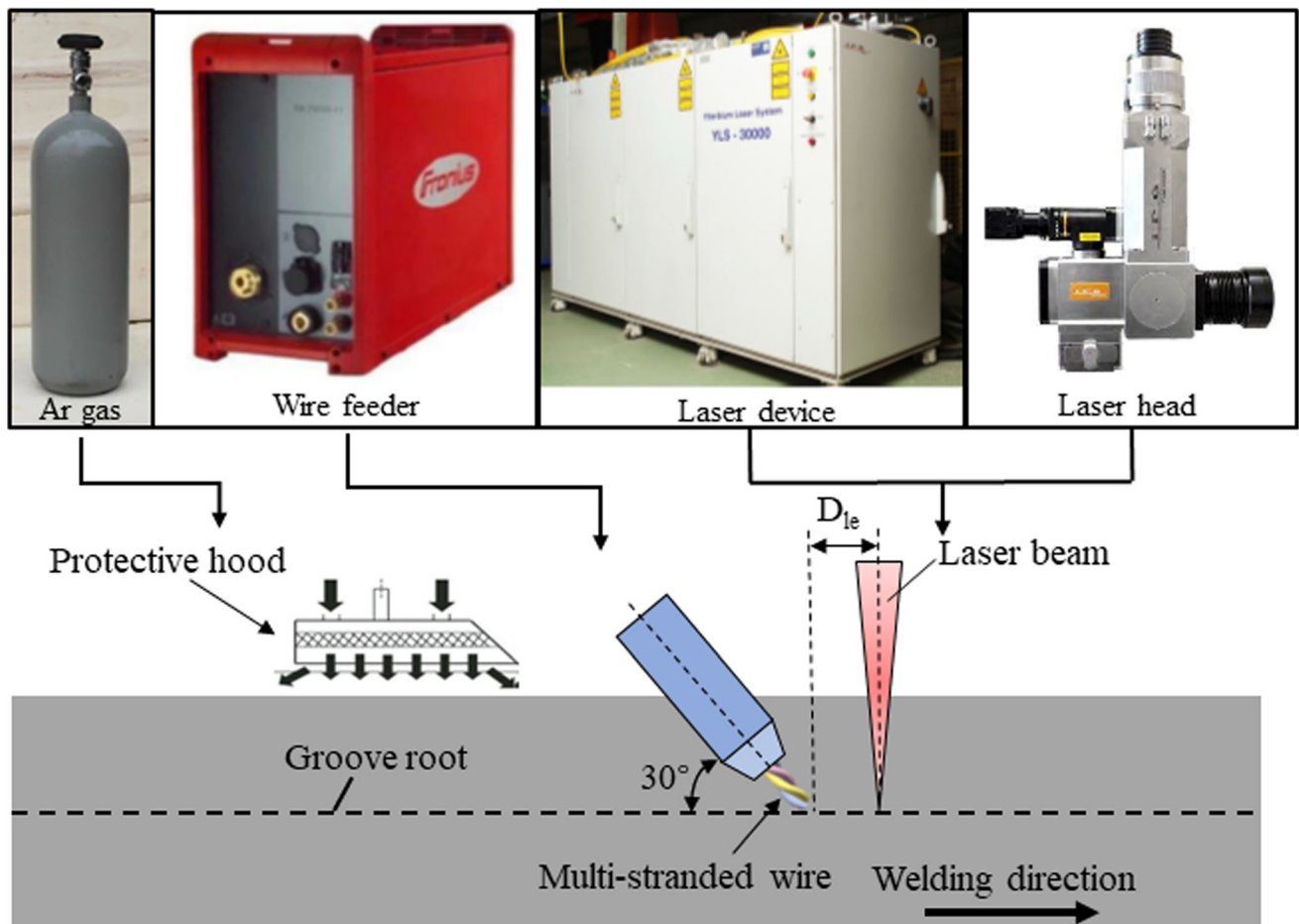
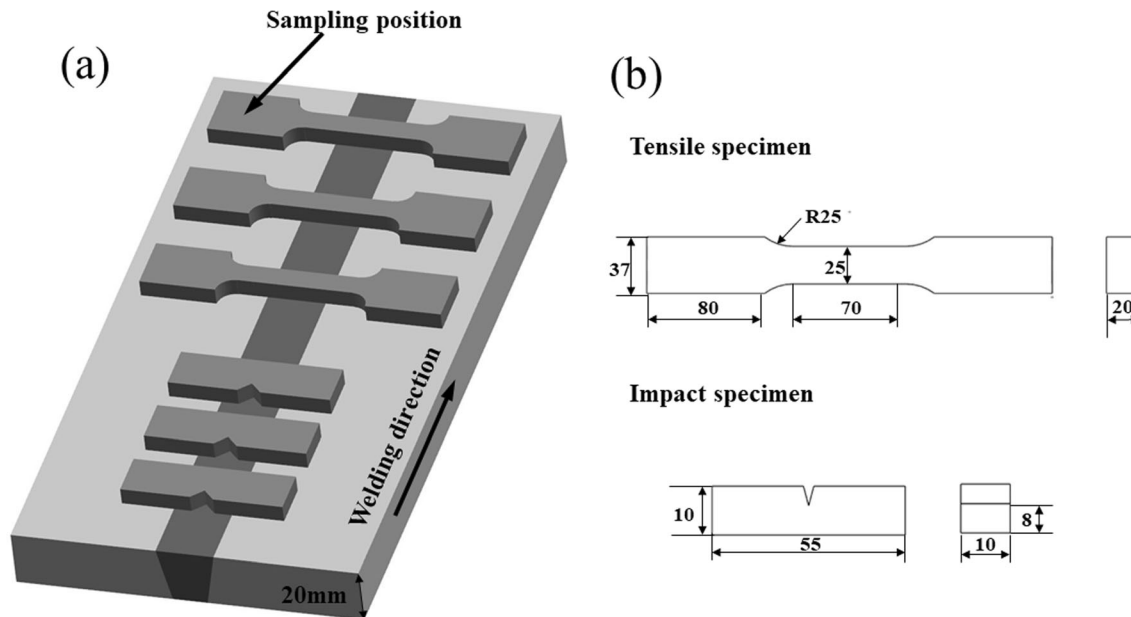


Fig. 1 Schematic diagram of the welding process



**Fig. 2** Schematic diagram of sampling position and size of tensile and impact (a) sampling position and (b) sampling size (unit: mm)

EVO 18), and transmission electron microscopy (TEM, model: FEI Talos F200X). The micro-Vickers hardness (model: HVS-1000Z) curve covered the joint from the welded metal (WM) in the center to the base metal (BM) in the right, measured with dots in an interval of 0.4 mm. The force in the test was 500 g, which was held for 10 s. A schematic diagram of the sampling position and size of tensile and impact is shown in Fig. 2. Tensile test at room temperature was carried out according to the standard EN ISO 4136:2011. Impact test at room temperature was carried out according to the standard EN ISO 9016:2012. Figure 2(a) shows the sampling position of tensile and impact. Figure 2(b) shows the sampling size of tensile and impact. The tensile test was carried out at room temperature using an AG-X PLUS electron-tensile tester at a 1 mm/min rate, and a room-temperature impact test was carried out with JB-300B.

### 3. Results and Discussion

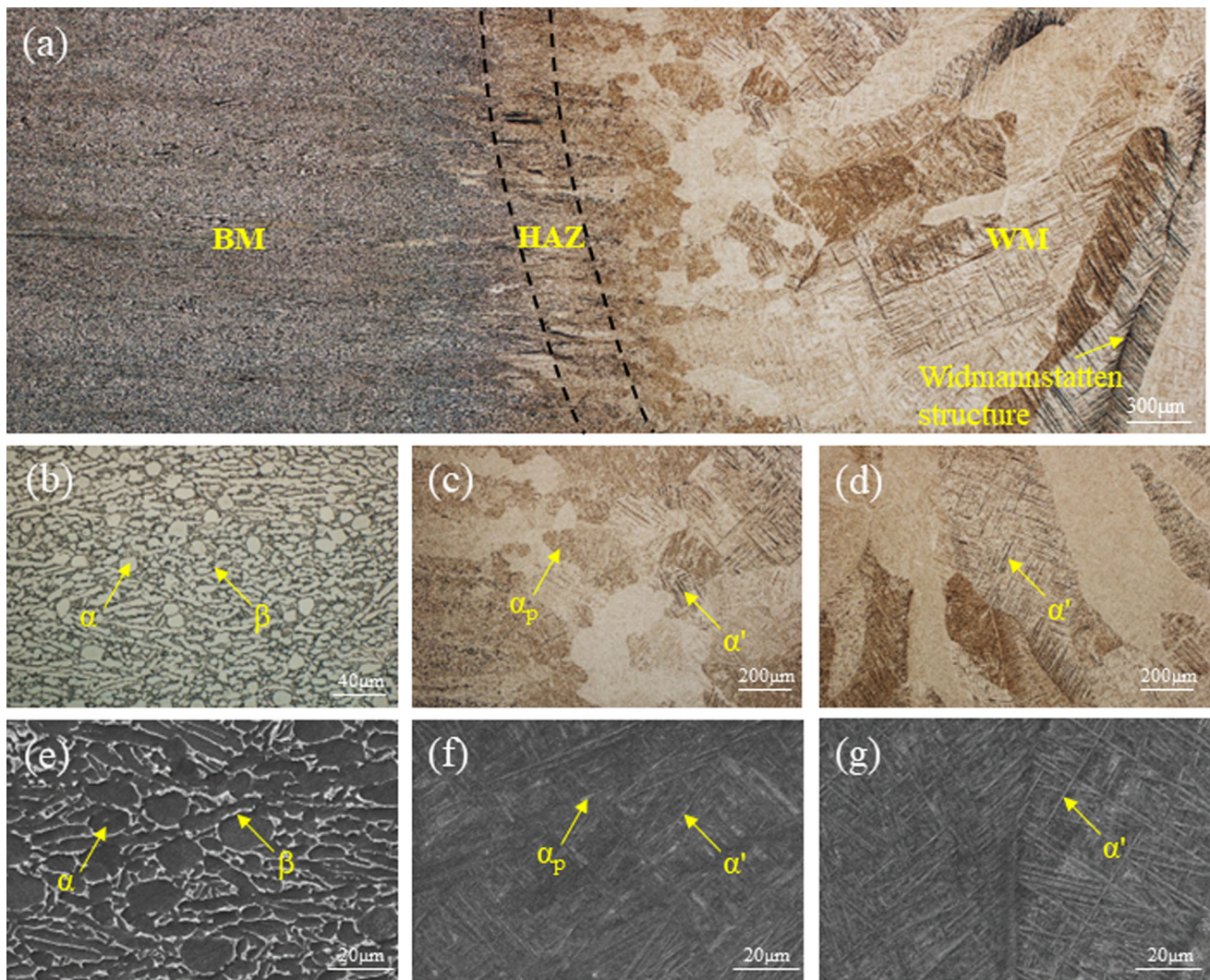
#### 3.1 Microstructure

Figure 3 and 4 shows the microstructure of as-welded and high-temperature annealing joints examined with OM and SEM techniques. Figure 3(a) and 4(a) shows the microstructure of as-welded and high-temperature annealing joints examined with OM. Though grain size varies significantly in each zone of the welded joints, as can be seen, they tend to grow from BM to WM. The melting point of titanium alloy requires large heat input during laser welding. The titanium plate was thick; thus, the cooling of the welded joints was fast and uneven. The microstructure of the WM showed typical casting microstructure characteristics: coarse columnar crystals grew from both sides of the low-temperature zone to the center of the welded seam. Besides, the widmanstatten structure of joints as-welded was found at the center of the welded seam.

Figure 3(b) and (e) shows the OM and SEM images of the microstructure of BM as-welded. The BM is mainly composed

of evenly distributed equiaxed  $\alpha$ -phase, a small amount of elongated  $\alpha$ -phase generated during the rolling process, and  $\beta$ -phase that is evenly distributed and attached to  $\alpha$ -phase; Fig. 4(b) and (e) shows the OM image of the microstructure and SEM morphology of the BM after high-temperature annealing. The BM is dual phase and composed of equiaxed  $\alpha$ -phase, secondary  $\alpha$ -phase, and  $\beta$ -phase. Compared with the BM as-welded, the size of the equiaxed  $\alpha$ -phase is more uniform, and the  $\beta$ -phase becomes smaller after heat treatment. At the same time, the elongated  $\alpha$ -phase generated during rolling also disappears. Figure 3(c) and (f) shows the OM and SEM images of the microstructure of the heat-affected zone (HAZ) as-welded. The HAZ mainly consists of a small amount of initial  $\alpha_p$  phase and  $\alpha'$  martensite, and there is few acicular  $\alpha'$  martensite in this zone. The microstructure of HAZ is also finer than that of WM. Figure 4(c) and (f) shows the OM image and SEM image of the microstructure of HAZ after high-temperature annealing. This zone is mainly composed of long acicular  $\alpha$ -phase and  $\beta$ -phase. Figure 3(d) and (g) shows the OM image and SEM image of the microstructure of the WM as-welded. This zone is full of messy distributed acicular primary  $\alpha'$  martensite throughout the columnar crystalline  $\beta$ -phase, which finally forms a basketweave microstructure. Among the intricate primary  $\alpha'$  martensite, a small amount of short secondary  $\alpha'$  martensite is found. The primary  $\alpha'$  martensite is formed at the early stage of  $\beta$ -phase solidification, while secondary  $\alpha'$  martensite is formed at the late stage, thus becoming shorter due to weak solidification driving force. Figure 4(d) and (g) shows the OM image and SEM image of the microstructure of the WM after high-temperature annealing. This zone is full of coarsened  $\alpha + \beta$  sheets, and the grain boundaries are clearer.

Figure 5 shows the inverse pole figure (IPF) image of the phase distribution of the welded zone as-welded and after heat treatment, respectively. When comparing Fig. 5(a) with (c), it can be found that phases with different orientations interwoven in the welded zone, while after heat treatment, they are less interweaved. Researchers (Ref 14-15) have indicated that



**Fig. 3** Microstructure of as-welded joints examined with OM and SEM (a) overall micromorphology, OM of the (b) BM, (c) HAZ and (d) WM, SEM of the (e) BM, (f) HAZ and (g) WM

anisotropic materials are more efficient in resisting crack propagation than isotropic materials, which helps to improve the toughness. The comparison also shows that the acicular lamellae grow thicker in the weld after heat treatment, and its length-to-diameter ratio decreases. The morphology of the lamellar phase will affect the properties of the alloy, and the growing thickness of the lamellar phase will reduce the tensile strength and hardness (Ref 16).

From Fig. 5(a), it can be found that the welded seam after heat treatment consists of small-size, big length-width ratio acicular  $\alpha'$  martensite, a small amount of residual  $\beta$ -phase, and a small amount of granular  $\beta$ -phase. From Fig. 5(b), it can be found that the welded zone as-welded consists mainly of  $\alpha'$  martensite (shown in red with 99.33% content) and a small amount of residual  $\beta$ -phase (shown in yellow with 0.67% content). After heat treatment, the  $\alpha$ -phase content of the welded seam decreases (shown in red with 98.66% content), and the  $\beta$ -phase content increases (shown in yellow with 1.34% content). Related studies show that when the annealing temperature is set within the  $\alpha + \beta$ -phase zone, the  $\alpha'$  martensite will decompose and form a granular  $\beta$ -phase at the

dislocations or laminated  $\beta$ -phase at the martensite boundary. Therefore, laminae  $\beta$ -phase exists between  $\alpha$ -phases (Ref 29).

In order to better understand the microstructures and properties of the welded joints as-welded and after heat treatment, the microstructure of the welded zone was examined and analyzed using the TEM technique. Figure 6(a) shows the microstructure of the welded zone using the TEM technique. As seen in Fig. 6(a), there are a number of lath  $\alpha'$  martensite with different orientations. During the laser welding process, with the increase of heat input,  $\beta$ -phase transformation will occur in the TC4 titanium alloy. Thus,  $\beta$  grains grow and coarsen rapidly. Due to the rapid cooling of the liquid melt pool, the grown and coarsened  $\beta$ -phase, being not able to diffuse and transform to  $\alpha$ -phase, shear transforms to  $\alpha'$  martensite, which is with the same crystal structure but different morphology of  $\alpha$ -phase (Ref 30). These  $\alpha'$  martensite interlaced with each other in a basketweave morphology. The width of the lath within the viewing field is  $0.59 \mu\text{m}$ , and there are also dislocations in part of the lath martensite  $\alpha'$ . Figure 6(b) shows the welded zone microstructure after high-temperature annealing using the TEM technique. As seen in Fig. 6(b), there is lamellar  $\alpha$ -phase in the microstructure, and when the annealing

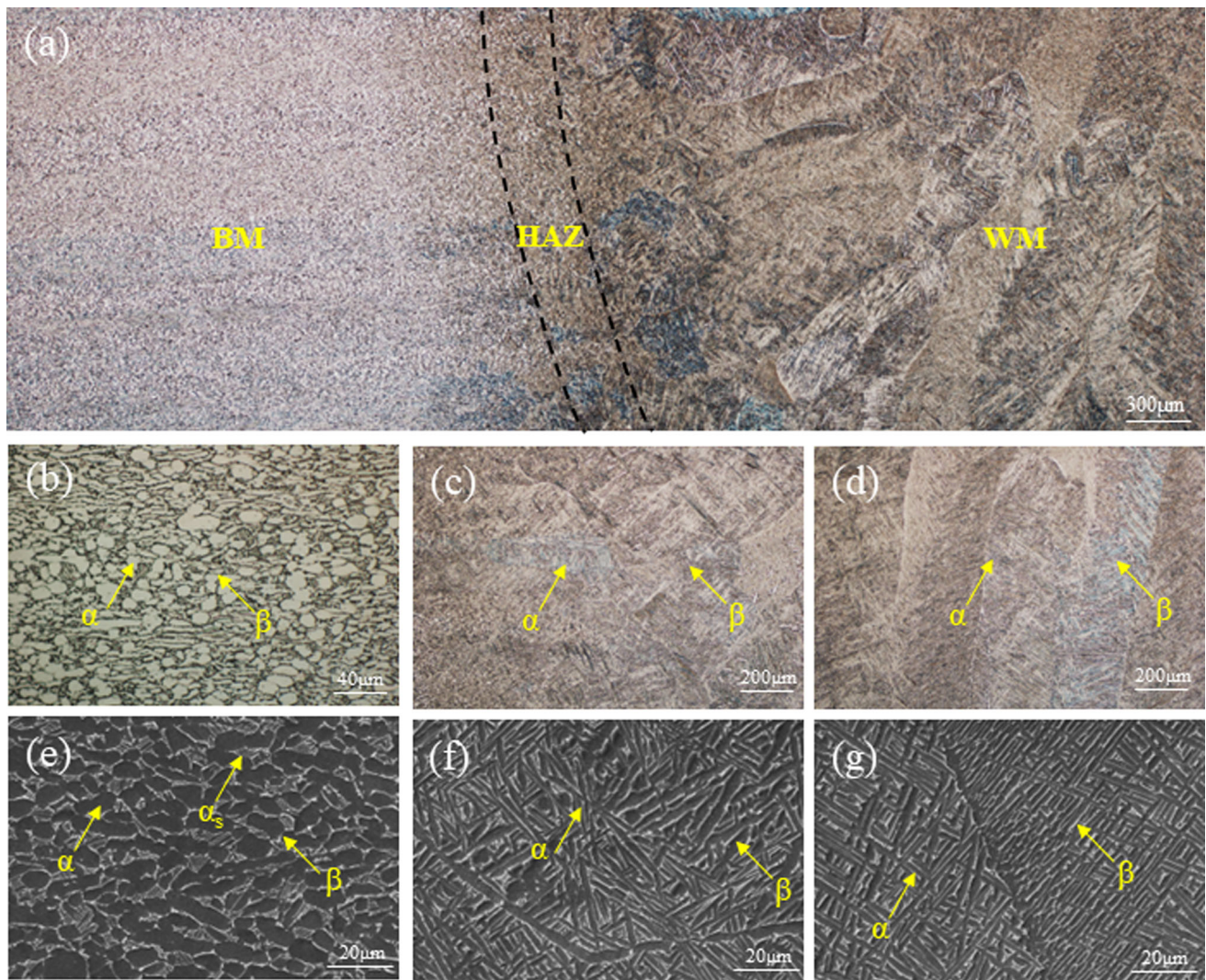


**Fig. 4** Microstructure of high-temperature annealing joints examined with OM and SEM (a) overall micromorphology, OM of the (b) BM, (c) HAZ and (d) WM, SEM of the (e) BM, (f) HAZ and (g) WM

is performed at 850 °C, which is within the  $\alpha + \beta$ -phase zone, the  $\alpha'$  martensite will decompose, generating lamellar  $\alpha$ -phase with lath width of 1.39  $\mu\text{m}$  in the field of view. The width of the  $\alpha$ -phase increased by 1.35 times compared with that of as-welded. In addition, dislocation density within the  $\alpha$ -phase is also significantly decreased.

For an in-depth understanding of the deformation of the as-welded and high-temperature annealing joints, quantitative analysis on the probability of slip system initiation was performed in the welded of the two groups of welded seam with the EBSD test technique. It is known that Schmid factor (SF) describes the initiation of the slip system in a given direction for crystal materials (Ref 29). Figure 7 shows the SF images and diagrams of the main phases of as-welded and high-temperature annealing joints. Figure 7(c) and (d) shows that 29.1% of the  $\alpha'$  martensite as-welded is with SF less than 0.15, and 25.9% is with SF between 0.4-0.5, while for high-temperature annealing ones, 14.1% martensite is with SF less than 0.15, and 42.9% is with SF between 0.4 and 0.5. The SF is higher for the as-welded joint than that of high-temperature annealing ones. Thus, the strength of  $\alpha'$  martensite of the as-

welded joint is better than that of the high-temperature annealing joint.

### 3.2 Mechanical Properties

**3.2.1 Microhardness.** Figure 8 shows the microhardness distribution of as-welded and high-temperature annealing joints. It can be found that the microhardness values of each joint are symmetrically distributed along the central axis of the welded seam. The microhardness values of WM, HAZ, and BM were 345 HV, 323 HV, and 295 HV for the as-welded joint, respectively. The microhardness value of WM and HAZ is higher than that of BM and fluctuates from WM, HAZ, to BM, particularly in HAZ, while after high-temperature annealing, the microhardness values of WM, HAZ, and BM were 334 HV, 313 HV, and 304 HV, respectively. Compared with the data of the as-welded joint, the microhardness of WM and HAZ decreased by 3.2 % and 3.1 %, respectively, and the microhardness of BM increased by 3.0 %. Besides, the fluctuation of microhardness among the three zones also abated. Such results may be because the varying microhardness values of welded

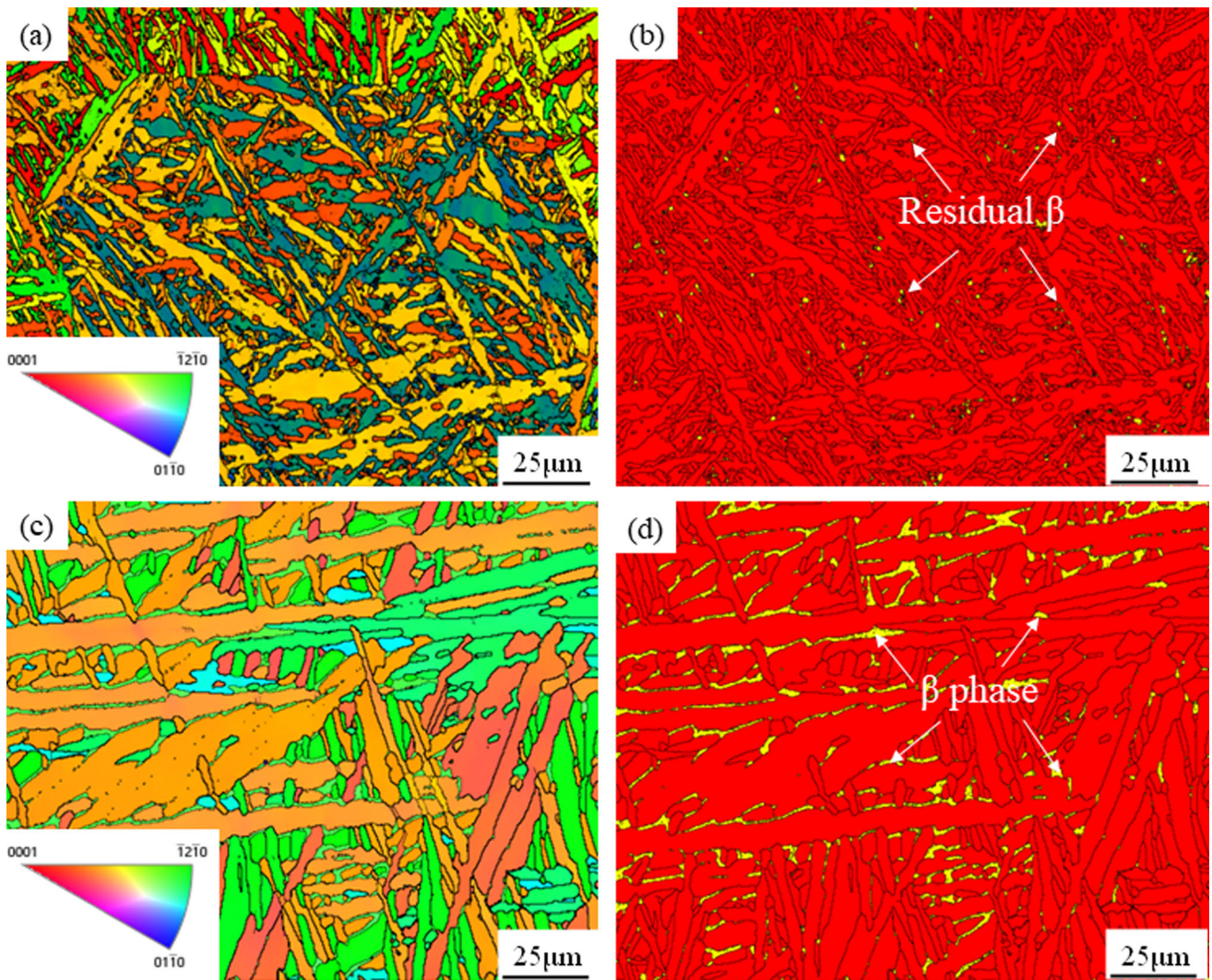


**Fig. 5** IPF image for (a) as-welded and (c) high-temperature annealing state, phase distribution for (b) as-welded and (d) high-temperature annealing state

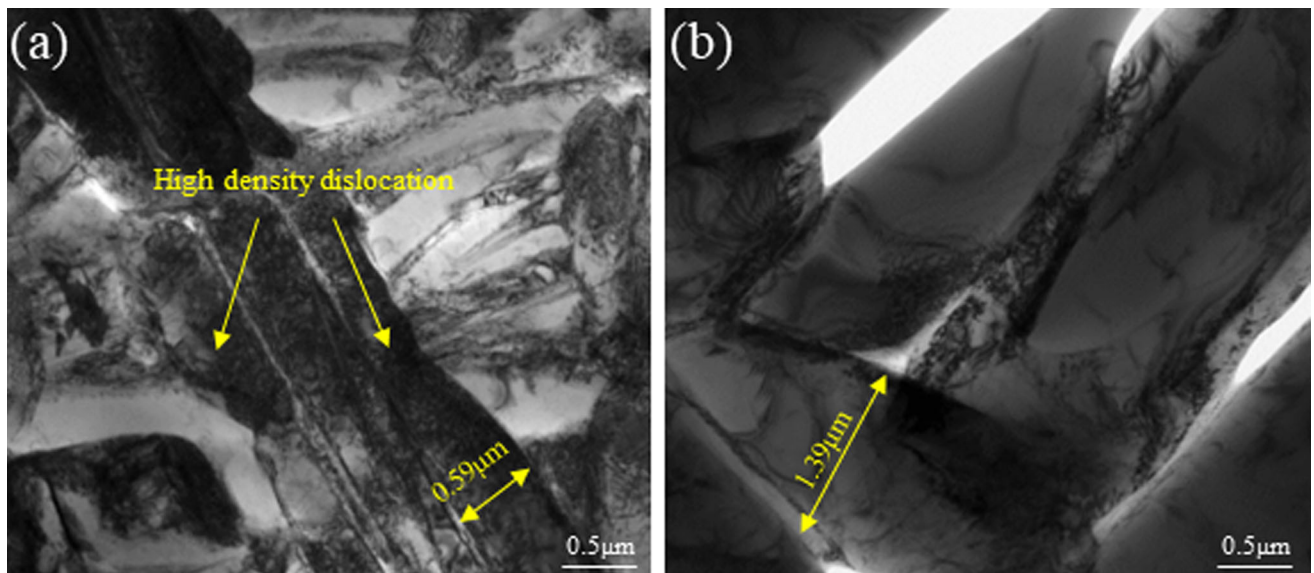


**Fig. 6** TEM microstructure morphology for (a) as-welded and (b) high-temperature annealing state

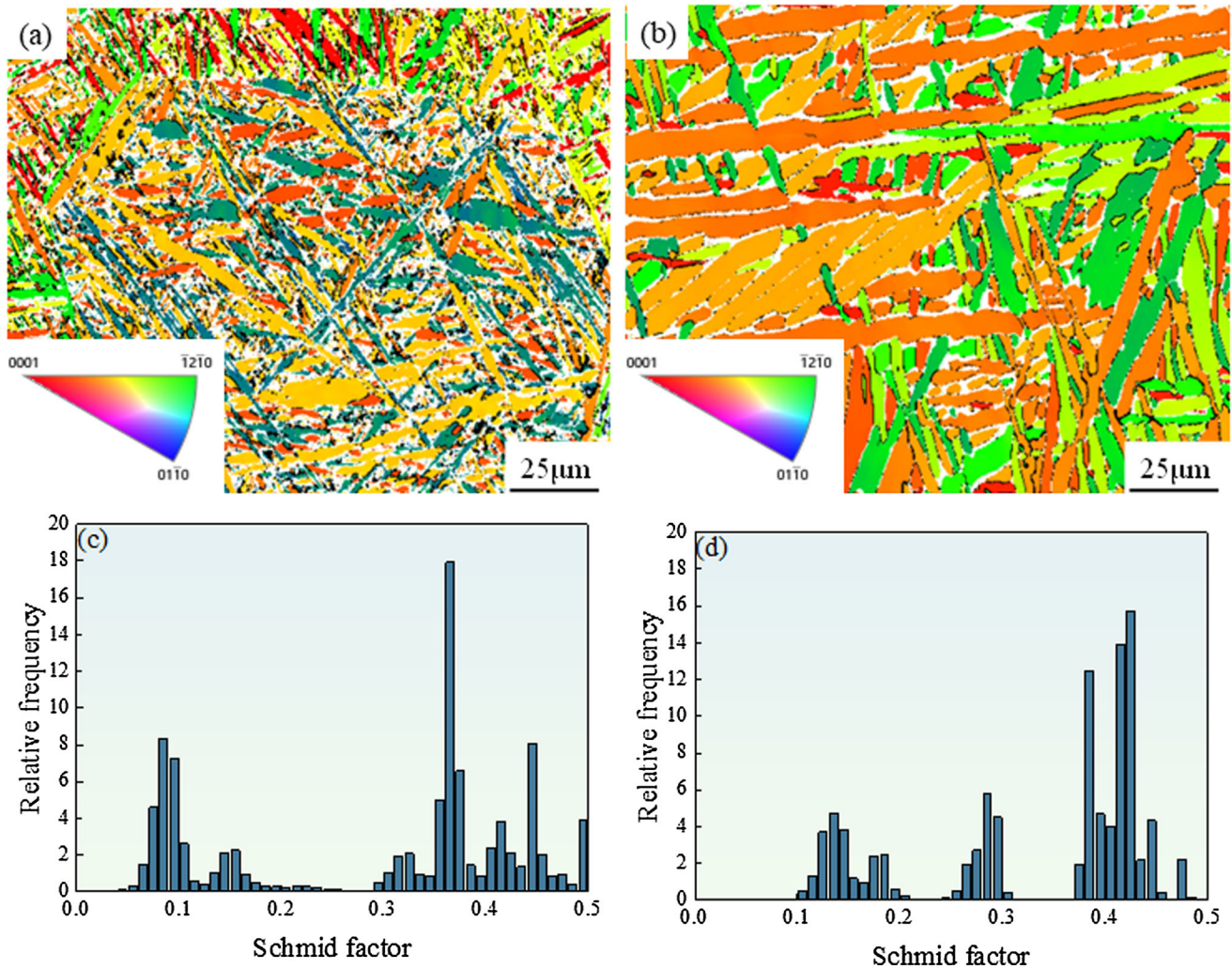


**Fig. 7** Distributions of  $\alpha$  for (a) as-welded and (b) high-temperature annealing state, SF of  $\alpha$  for (c) as-welded and (d) high-temperature annealing state

joints are related to the microstructures of BM, HAZ, and WM. Related studies (Ref 25) indicated that the microhardness of titanium alloys follows the rule of  $\alpha' > \alpha > \beta$ . The microstructures of the as-welded joint from WM, HAZ, to BM were a great amount of acicular  $\alpha'$  martensite, a few initial  $\alpha_p$  phases,  $\alpha'$  martensite, evenly distributed equiaxed  $\alpha$ -phase, and a small number of  $\alpha$ -phase and  $\beta$ -phase, respectively. As indicated in Fig. 6,  $\alpha'$  martensite features a high density of dislocations and subgrain boundaries. Therefore, the microhardness value would be greater when approaching closer to the center of the welded seam. High-temperature annealing joint occurred  $\alpha'$  martensite decomposition, so the fluctuations in the microhardness reduced significantly.

**3.2.2 Tensile Strength.** Table 1 shows the test results of the tensile properties of the BM and welded joints. The average tensile strength of the welded joints and BM as-welded was 941 MPa and 925 MPa, respectively. The elongation rate of the joint was only 11.0%, about 88% of the BM; for a high-temperature annealing joint, the average tensile strength was 902 MPa, with an elongation rate of 14.5%. Compared with the as-welded joint, the elongation rate of high-temperature annealing joint has increased 3.5%, with tensile strength

reduced by only about 4.1%, indicating a satisfactory performance of the tensile strength and plasticity. Tensile specimens fracture location of as-welded and high-temperature annealing joints is shown in Fig. 9. A tensile fracture appeared at the BM of the as-welded joint. As for high-temperature annealing joint, the fracture occurred at WM.

Figure 10 shows the fracture morphology of the tensile specimen of as-welded and high-temperature annealing joints. Both fractures were ductile. The fracture of the as-welded joint was with shallow dimple and cleavage, while the other was with deeper and wider dimples, inside which tiny dimples could also be found. It may be due to the different microstructures of the WM and BM. During the tensile process, the deformation of WM and BM was uncoordinated: brittle phase  $\alpha'$  martensite in the BM has reduced plasticity though strength was improved. Under tensile stress, the deformation of BM resulted in hardening, so the tensile strength of the WM was better than that of the BM, while deformation in WM was slight, resulting in a low elongation rate of the WM.

$\alpha'$  martensite, after high-temperature annealing, will transform to lamellar  $\alpha + \beta$  phase, of which  $\beta$ -phase belongs to the dense row of hexagonal and with more slip systems than  $\alpha'$  martensite has. In addition, as shown in Fig. 7, the SF of the  $\alpha$

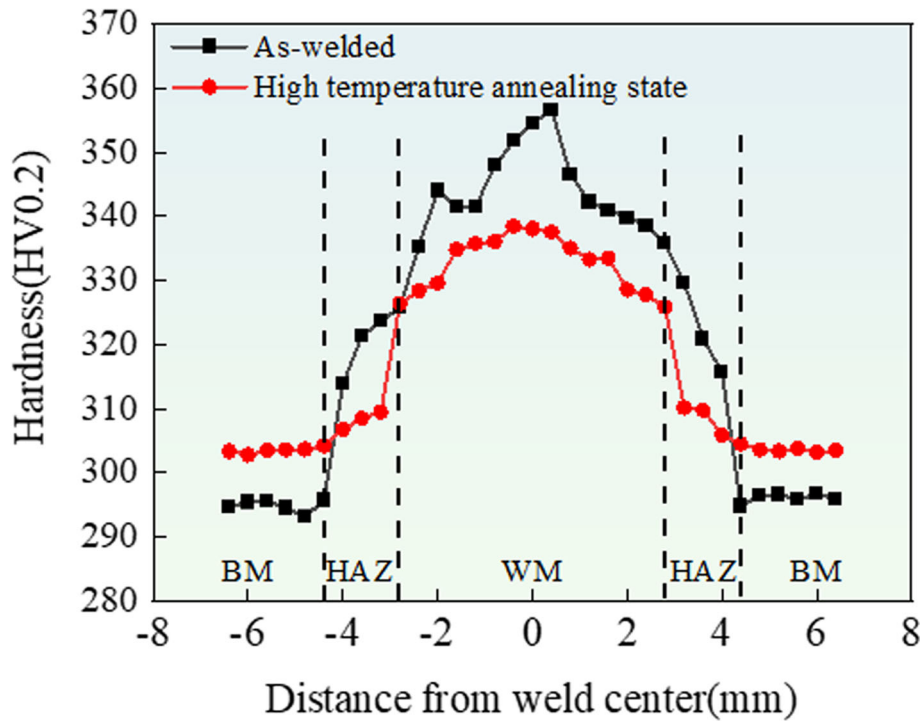


Fig. 8 Microhardness in welded cross section of as-welded and high-temperature annealing state

Table 1 Tensile properties of BM and welded joint for TC4 titanium alloy

Test sample	State	Value	Tensile strength, MPa	Elongation rate, %	Failed location
BM	...	Measured Average	912, 928, 935 925	12.5, 12.5, 13.0 12.5	...
Joint-1	As-welded	Measured Average	935, 940, 945 941	10.5, 11.0, 11.5 11.0	BM
Joint-2	High-temperature annealing state	Measured Average	898, 904, 906 902	14.5, 14.5, 15.0 14.5	WM

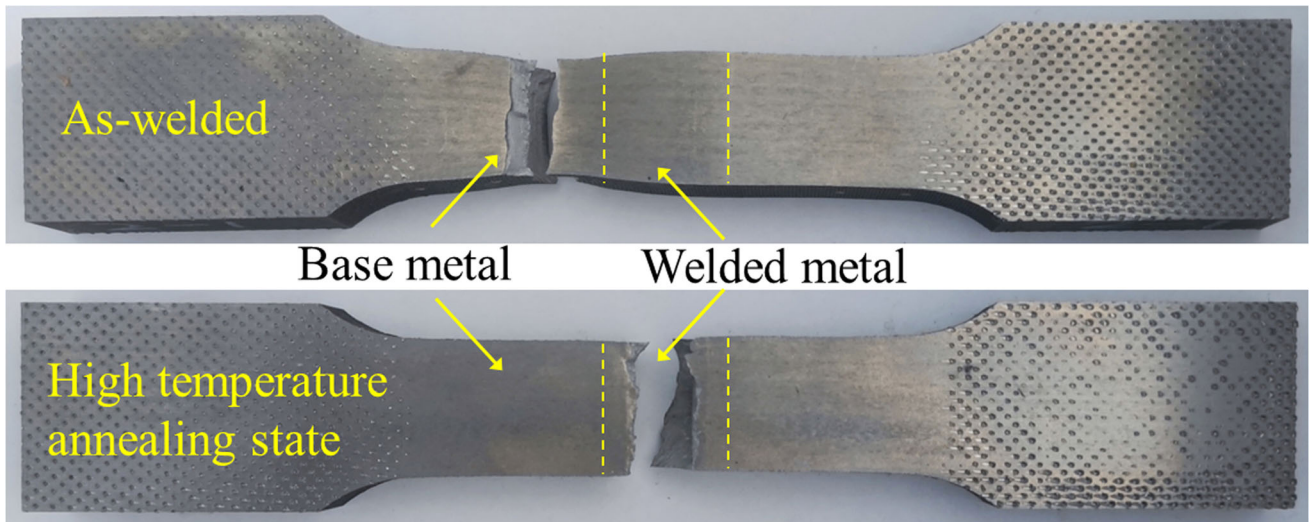
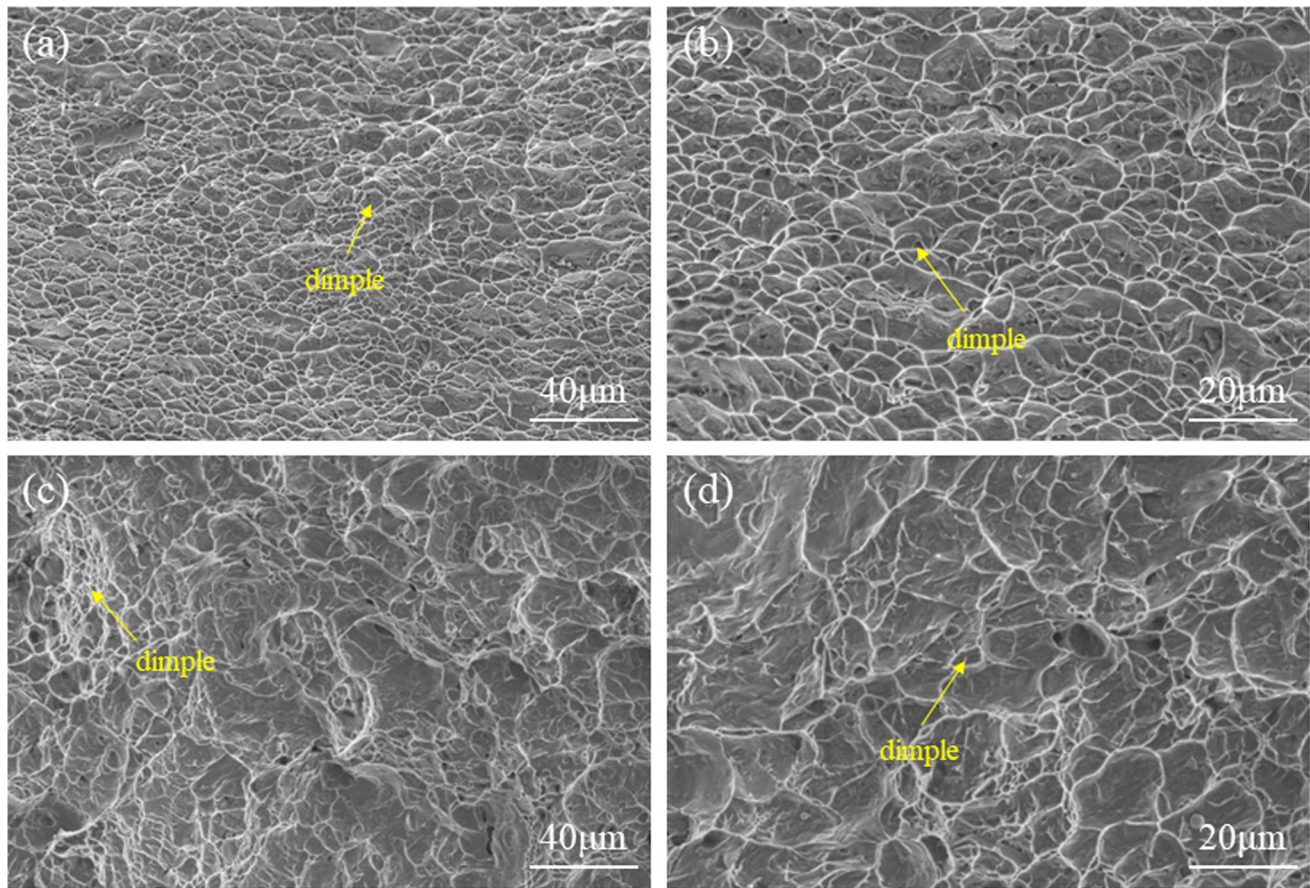


Fig. 9 Tensile specimen fracture location of as-welded and high-temperature annealing welded joints



**Fig. 10** Fracture morphology of tensile specimens for (a) low and (b) high magnification of as-welded, (c) low and (d) high magnification of high-temperature annealing state

phase of the as-welded joint is higher than that of high-temperature annealing one, so the probability of slip system initiation is bigger. Lastly, the  $\alpha$ -phase lath thickness of high-temperature annealing joint increased by about 800 nm compared to the as-welded joint. Related studies have proved a Hall–Petch relationship between post-break elongation and lath thickness of welded joints: the post-break elongation rate will increase with lath thickness. Therefore, it explains why the welded joints strength decreased and the plasticity improved after high-temperature annealing (Ref 31-32).

**3.2.3 Impact Toughness.** The impact test performance of V-notch under room temperature is shown in Fig. 11. The impact toughness of WM as-welded is 12 J, and high-temperature annealing is 18.5 J, increased by about 54%. The impact toughness of WM is improved significantly.

Figure 12 shows the impact fracture morphology of WM as-welded and with high-temperature annealing state. The impact fracture of the as-welded joint has shallower dimples. In contrast, the high-temperature annealing impact fracture has deeper dimples. The influence mechanism of impact toughness is very complicated. The content, morphology, and size of  $\alpha'$  martensite,  $\alpha$ -phase, and  $\beta$ -phase will strongly influence the impact toughness. The above results may be due to the high content of acicular  $\alpha'$  martensite in the as-welded joint.  $\alpha'$  martensite with a brittle phase tends to be a crack source during the impact process, which allows the crack to propagate through a low-energy path.  $\alpha'$  martensite has provided such a path due to its small size, which requires less energy for a crack

to pass through than to steer direction or bifurcation. High-temperature annealing has coarsened the  $\alpha$ -phase, requiring more energy for the crack to pass through than to steer direction or bifurcate. Thus, the crack bypassed and propagated along the lamellar  $\alpha$ -phase or  $\alpha/\beta$  grain boundaries, presenting a zigzagging cracking path. In this way, the impact properties were improved significantly (Ref 33-34).

## 4. Conclusions

After narrow gap laser welding of TC4 titanium alloy with wire feed, this study performed high-temperature annealing of the welded joint to improve its microstructure and mechanical properties. It further revealed the relationship between microstructure and mechanical properties. The main conclusions are as follows:

- (1) After high-temperature annealing at 850 °C/2 h, supersaturated  $\beta$ -columnar crystals and acicular  $\alpha'$  martensite of the WM decompose to lamellar  $\alpha$  and  $\beta$ -phase. The content of the  $\alpha$ -phase decreased, and  $\beta$ -phase increased compared with that of as-welded. The  $\alpha$ -phase width increased by 1.35 times, the internal dislocation density decreased sharply, and the probability of slip system initiation increased.

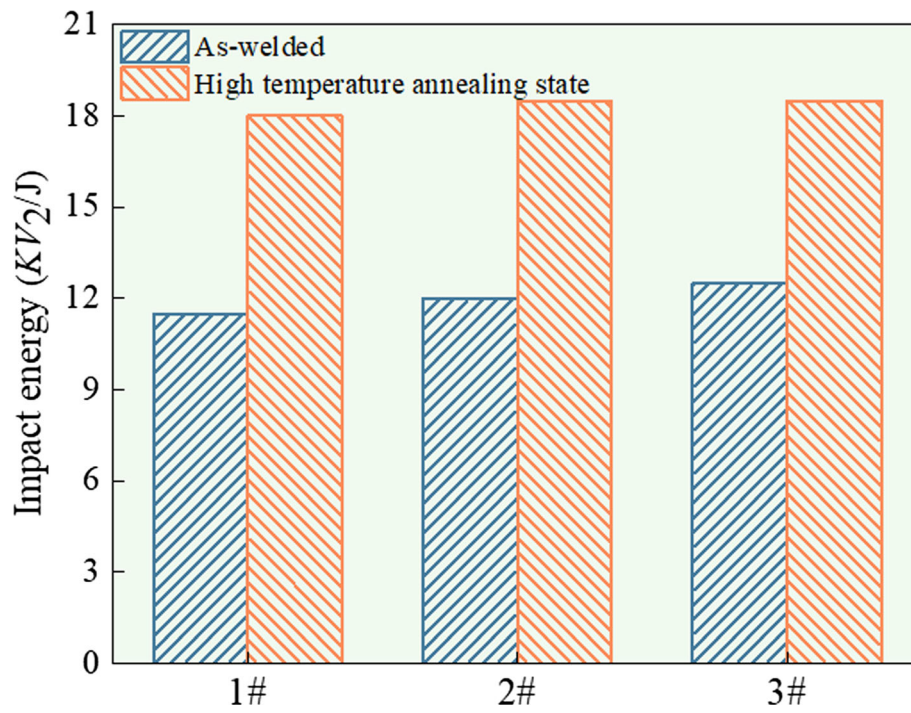


**Fig. 11** Charpy impact energy comparison histogram of as-welded and high-temperature annealing state

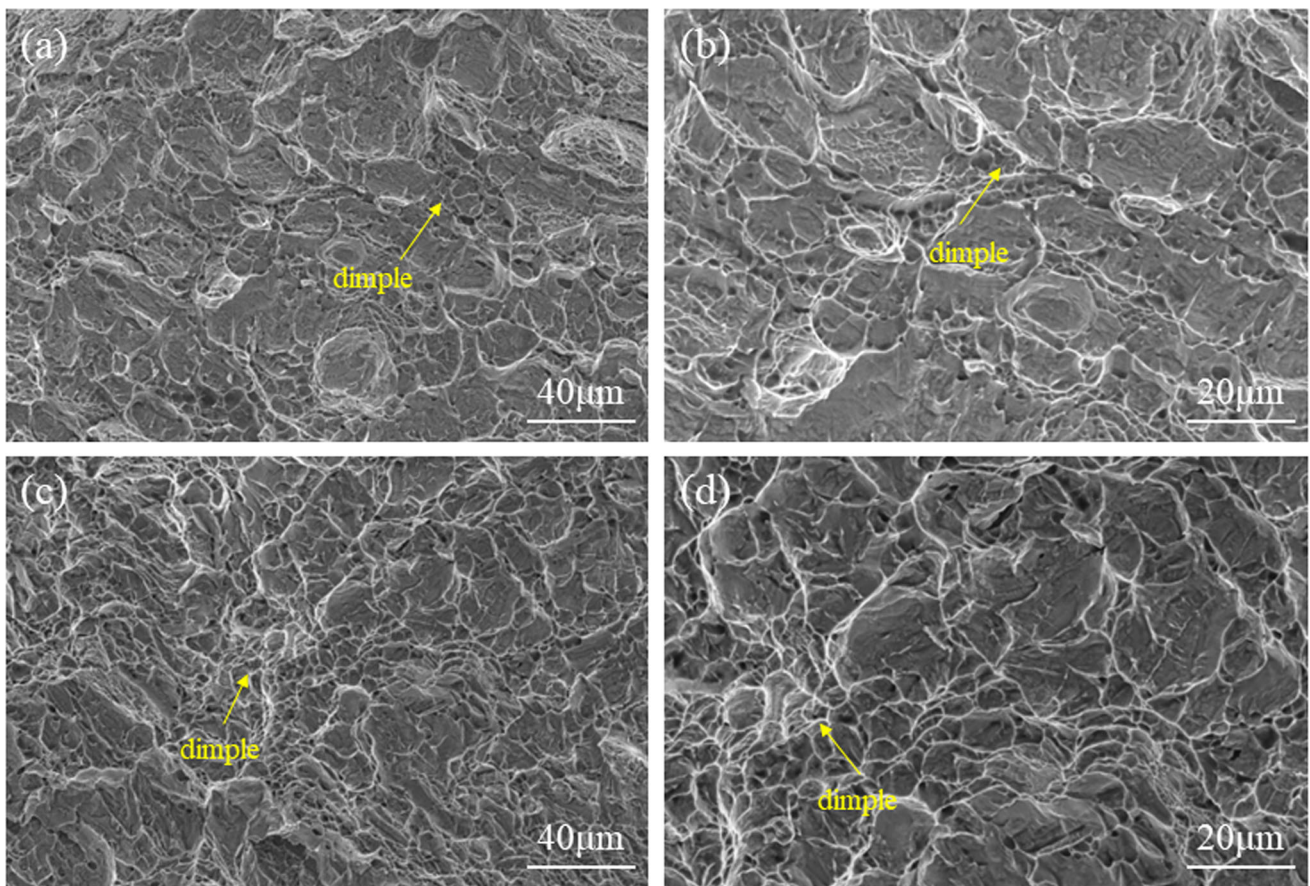


**Fig. 12** Fracture morphology of impact specimens for (a) low and (b) high magnification of as-welded, (c) low and (d) high magnification of high-temperature annealing state

- (2) The microhardness of WM, HAZ, and BM of the as-welded joint was 345 HV, 323 HV, and 295 HV, respectively. Different microstructures of WM, HAZ, and BM caused fluctuations in the microhardness of the as-welded. After high-temperature annealing, the microhardness of WM and HAZ reduced by 3.2 % and 3.1 %, respectively, while that of BM increased by 3.0 %, and the fluctuation of microhardness values also abated in different joint zones.
- (3) The average tensile strength of WM the as-welded joint was 941 MPa, respectively, and the elongation rate was only 11.0%, impact toughness only 12 J. After high-temperature annealing state, the average tensile strength of the WM was 902 MPa, and the elongation rate was 14.5%, with about a 4.1% decrease in tensile strength and a 3.5% increase in elongation rate, showing satisfactory strength and plasticity performance. the impact strength grew to 18.5 J, increasing by about 54%.

## References

1. C.L. Jia, L.H. Wu, P. Xue, D.R. Ni, B.L. Xiao and Z.Y. Ma, Effect of Static Annealing on Superplastic Behavior of a Friction Stir Welded Ti-6Al-4V Alloy Joint and Its Microstructural Evolution (In English), *J. Mater. Sci. Technol.*, 2022, **130**, p 112–123. <https://doi.org/10.1016/j.jmst.2022.05.006>
2. H.B. Xia, C.W. Tan, L.Q. Li and N.S. Ma, In Situ SEM Study on Tensile Fractured Behavior of Al/Steel Laser Welding-brazing Interface (In English), *J. Mater. Eng. Perform.*, 2018, **27**, p 1047–1057. <https://doi.org/10.1007/s11665-018-3227-8>
3. M. Bambach, I. Sizova, J. Szyndler, J. Bennett, G. Hyatt, J. Cao, T. Papke and M. Merklein, On the Hot Deformation Behavior of Ti-6Al-4V Made by Additive Manufacturing (In English), *J. Mater. Process. Technol.*, 2021, **288**, p 116840. <https://doi.org/10.1016/j.jmatprotec.2020.116840>
4. J.S. Jha, S.P. Toppo, R. Singh, A. Tewari and S.K. Mishra, Deformation Behavior of Ti-6Al-4V Microstructures Under Uniaxial Loading: Equiaxed Vs. Transformed- $\beta$  Microstructures (In English), *Mater. Charact.*, 2021, **171**, p 110780. <https://doi.org/10.1016/j.matchar.2020.110780>
5. J.K. Huang, Y.Q. Huang, X.Q. Yu, G.Y. Liu, S.R. Yu and D. Fan, Corrosion Characterization of Ti-6Al-4V Coating Layer by The Alternating Current Assisted GTAW Method, *Corros. Sci.*, 2022, **197**, p 110066. <https://doi.org/10.1016/j.corsci.2021.110066>
6. C.L. Jia, L.H. Wu, P. Xue, H. Zhang, D.R. Ni, B.L. Xiao and Z.Y. Ma, Static Spheroidization Behavior and Its Effect on Superplasticity of Fine Lamellae in Nugget of a Friction Stir Welded Ti-6Al-4V Joint (In English), *J. Mater. Sci. Technol.*, 2022, **119**, p 1–10. <https://doi.org/10.1016/j.jmst.2021.10.054>
7. S.M. Kelly and S.L. Kampe, Microstructural Evolution in Laser-deposited Multilayer Ti-6Al-4V Builds: Part II. Thermal Modeling, *Metall. Mater. Trans. A*, 2004, **35**, p 1869–1879.
8. M. Balasubramanian, V. Jayabalan and V. Balasubramanian, Effect of Pulsed Gas Tungsten Arc Welding on Corrosion Behavior of Ti-6Al-4V Titanium Alloy (In English), *Mater. Des.*, 2008, **29**, p 1359–1363. <https://doi.org/10.1016/j.matdes.2007.06.009>
9. X. Wen, M.P. Wan, C.W. Huang and M. Lei, Strength and Fracture Toughness of TC21 Alloy with Multi-level Lamellar Microstructure (In English), *Mater. Sci. Eng. A*, 2019, **740**, p 121–129. <https://doi.org/10.1016/j.msea.2018.10.056>
10. P. Åkerfeldt, M.L. Antti and R. Pederson, Influence of Microstructure on Mechanical Properties of Laser Metal Wire-Deposited Ti-6Al-4V (In English), *Mater. Sci. Eng. A*, 2016, **674**, p 428–437. <https://doi.org/10.1016/j.msea.2016.07.038>
11. J. Ju, J. Li, C. Yang, K. Wang, M. Kang and J. Wang, Evolution of The Microstructure and Optimization of The Tensile Properties of The Ti-6Al-4V Alloy by Selective Laser Melting and Heat Treatment (In English), *Mater. Sci. Eng. A*, 2021, **802**, p 140673. <https://doi.org/10.1016/j.msea.2020.140673>
12. S. Liu and Y.C. Shin, Additive Manufacturing of Ti6Al4V Alloy: A Review (In English), *Mater. Des.*, 2019, **164**, p 107552. <https://doi.org/10.1016/j.matdes.2018.107552>
13. N. Sareesh, M. Gopalakrishna Pillai and J. Mathew, Investigations into The Effects of Electron Beam Welding on Thick Ti-6Al-4V Titanium Alloy (In English), *J. Mater. Process. Technol.*, 2007, **192**, p 83–88. <https://doi.org/10.1016/j.jmatprotec.2007.04.048>
14. C.Y. Zeng, Y.P. Zhang, J.L. Hu, B. Hou, C.L. Dong and Y. Zhou, The Role of Microstructure on Corrosion Fatigue Behavior of Thick-plate Ti-6Al-4V Joint Via Vacuum Electron Beam Welding (In English), *Vacuum*, 2020, **2020**(182), p 109714. <https://doi.org/10.1016/j.vacuum.2020.109714>
15. N.W. Fang, E.J. Guo, R.S. Huang, L.M. Yin, Y.S. Chen, C.Y. Zeng, H. Cao, J.P. Zou and K. Xu, Effect of Welding Heat Input on Microstructure and Properties of TC4 Titanium Alloy Ultra-narrow Gap Welded Joint by Laser Welding with Filler Wire (In English), *Mater. Res. Express*, 2021, **8**, p 016511. <https://doi.org/10.1088/2053-1591/abd4b3>
16. G. Li and C.Q. Sun, High-Temperature Failure Mechanism and Defect Sensitivity of TC17 Titanium Alloy in High Cycle Fatigue (In English), *J. Mater. Sci. Technol.*, 2022, **122**, p 128–140. <https://doi.org/10.1016/j.jmst.2022.01.010>
17. N.W. Fang, E.J. Guo, K. Xu, R.S. Huang, Y.M. Ma, Y.S. Chen, Y.C. Yang and J.L. Xie, In-situ Observation of Grain Growth and Phase Transformation in Weld Zone of Ti-6Al-4V Titanium Alloy by Laser Welding with Filler Wire (In English), *Mater. Res. Express*, 2021, **8**, p 056507. <https://doi.org/10.1088/2053-1591/abfc7b>
18. W.M. Long, D.S. Liu, A.P. Wu, D.C. Wang and G.Q. Huang, Influence of laser scanning speed on the formation property of laser brazing diamond coating, *Diam. Relat. Mater.*, 2020, **110**, p 108085. <https://doi.org/10.1016/j.diamond.2020.108085>
19. T. Yang, Y.H. Xiao, Y.A. Zhuang, J.Y. Liu, H.Y. Li and Y. Wang, Effect of Microstructural Heterogeneity on Corrosion Fatigue Crack Growth Behavior of 60-mm Thick-plate TC4 Titanium Alloy NG-GTAW Welded Joint (In English), *Int. J. Fatigue*, 2022, **163**, p 107030. <https://doi.org/10.1016/j.ijfatigue.2022.107030>
20. L.B. Sun, M.Q. Wang, L.J. Huang, N.W. Fang, P.B. Wu, R.S. Huang, K. Xu, X.X. Wang, J. Qin, S. Li and W.M. Long, Comparative Study on Laser Welding Thick-Walled TC4 Titanium Alloy with Flux-Cored Wire and Cable Wire (In English), *Materials*, 2023, **16**, p 1509. <https://doi.org/10.3390/ma16041509>
21. M.Q. Wang, N.W. Fang, L.B. Sun, P.B. Wu, R.S. Huang, K. Xu, X.X. Wang, J. Qin, Z.Z. Zhou, S. Li, J.H. Su and W.M. Long, Study of the Microstructure and Properties of the Butt Joint of Laser-Welded Titanium Alloy with Flux-Cored Wire (In English), *Metals-Basel*, 2023, **13**, p 369. <https://doi.org/10.3390/met13020369>
22. C.W. Huang, Y.Q. Zhao, S.W. Xin, W. Zhou, Q. Li, W.D. Zeng and C.S. Tan, High Cycle Fatigue Behavior of Ti-5Al-5Mo-5V-3Cr-1Zr Titanium Alloy with Bimodal Microstructure (In English), *J. Alloy. Compd.*, 2016, **695**, p 1966–1975. <https://doi.org/10.1016/j.jallcom.2016.11.031>
23. Y.L. Qi, J. Deng, Q. Hong and L.Y. Zeng, Electron Beam Welding, Laser Beam Welding and Gas Tungsten Arc Welding of Titanium Sheet (In English), *Mater. Sci. Eng. A*, 2000, **280**, p 177–181. [https://doi.org/10.1016/S0921-5093\(99\)00662-0](https://doi.org/10.1016/S0921-5093(99)00662-0)
24. G.Q. Wang, Z.Y. Chen, J.W. Li, J.R. Liu, Q.J. Wang and R. Yang, Microstructure and Mechanical Properties of Electron Beam Welded Titanium Alloy Ti-6246 (In English), *J. Mater. Sci. Technol.*, 2018, **34**, p 570–576. <https://doi.org/10.1016/j.jmst.2016.10.007>
25. T. Debroy, H. Wei, J. Zuback, T. Mukherjee, J. Elmer, J. Milewsko, A. Beese, A. Wilson, A. De and W. Zhang, Additive Manufacturing of Metallic Components- Process (In English), *Structure and Properties. Prog. Mater. Sci.*, 2018, **92**, p 112–224. <https://doi.org/10.1016/j.pmatsci.2017.10.001>
26. X.Y. Zhang, G. Fang, S. Leeftang, A.J. Böttger, A.A. Zadpoor and J. Zhou, Effect of Subtransus Heat Treatment on The Microstructure and Mechanical Properties of Additively Manufactured Ti-6Al-4V Alloy, *J. Alloys. Compd.*, 2018, **735**, p 1562–1575. <https://doi.org/10.1016/j.jallcom.2017.11.263>
27. S. Cao, R.K. Chu, X.G. Zhou, K. Yang, Q.G. Jia, C.V.S. Lim, A.J. Huang and X.H. Wu, Role of Martensite Decomposition in Tensile Properties of Selective Laser Melted Ti-6Al-4V (In English), *J. Alloys.*

- Compd.*, 2018, **744**, p 357–363. <https://doi.org/10.1016/j.jallcom.2018.02.111>
28. W. Xu, E.W. Lui, A. Pateras, M. Qian and M. Brandt, In Situ Tailoring Microstructure in Additively Manufactured Ti-6Al-4V for Superior Mechanical Performance (In English), *Acta Mater.*, 2017, **125**, p 390–400. <https://doi.org/10.1016/j.actamat.2016.12.027>
29. S.Q. Wu, Y.J. Lu, Y.L. Gan, T.T. Huang, C.Q. Zhao, J.J. Lin, S. Guo and J.X. Lin, Microstructural Evolution and Microhardness of A Selective-laser-melted Ti-6Al-4V Alloy After Post Heat Treatments (In English), *J. Alloys Compd.*, 2016, **672**, p 643–652. <https://doi.org/10.1016/j.jallcom.2016.02.183>
30. Z.L. Liang, Z.G. Sun, W.S. Zhang, S.K. Wu and H. Chang, The Effect of Heat Treatment on Microstructure Evolution and Tensile Properties of Selective Laser Melted Ti-6Al-4V Alloy (In English), *J. Alloys Compd.*, 2019, **782**, p 1041–1048. <https://doi.org/10.1016/j.jallcom.2018.12.051>
31. J.P. Shi, G. Song and J.Y. Chi, Effect of Active Gas on Weld Appearance and Performance in Laser-TIG Hybrid Welded Titanium Alloy (In English), *Int. J. Lightweight Mater. Manuf.*, 2018, **1**, p 47–53. <https://doi.org/10.1016/j.ijlmm.2018.03.002>
32. X.Z. Li, S.B. Hu, J.Z. Xiao and L.B. Ji, Effects of The Heterogeneity in The Electron Beam Welded Joint on Fatigue Crack Growth in Ti-6Al-4V Alloy (In English), *Mater. Sci. Eng. A*, 2011, **529**, p 170–176. <https://doi.org/10.1016/j.msea.2011.09.014>
33. A.M. Khorasani, I. Gibson, M. Goldberg and G. Littlefair, On The Role of Different Annealing Heat Treatments on Mechanical Properties and Microstructure of Selective Laser Melted and Conventional Wrought Ti-6Al-4V (In English), *Rapid. Prototyping. J.*, 2017, **23**, p 295–304. <https://doi.org/10.1108/RPJ-02-2016-0022>
34. Y.D. Liu, J.H. Liu, W.S. Gu, H.L. Li, W.H. Li, Z.L. Pei, J. Gong and C. Sun, Oxidation, Mechanical and Tribological Behaviors of The Ni/cBN Abrasive Coating-Coated Titanium Alloys (In English), *Acta. Metall. Sin.*, 2021, **36**, p 31–35. <https://doi.org/10.1007/s40195-020-01167-0>

**Publisher's Note** Springer Nature remains neutral with regard to jurisdictional claims in published maps and institutional affiliations.

Springer Nature or its licensor (e.g. a society or other partner) holds exclusive rights to this article under a publishing agreement with the author(s) or other rightsholder(s); author self-archiving of the accepted manuscript version of this article is solely governed by the terms of such publishing agreement and applicable law.